

The Pauli principle in a three-body cluster model and the momentum distributions after fragmentation of ${}^6\text{He}$ and ${}^{11}\text{Li}$

E. Garrido, D.V. Fedorov and A.S. Jensen
 Institute of Physics and Astronomy, Aarhus University,
 DK-8000 Aarhus C, Denmark
 (October 16, 2018)

We investigate two simple prescriptions to account for the Pauli principle in a three-body cluster model employing a new method based on an adiabatic hyperspherical expansion to solve the Faddeev equations in coordinate space. The resulting wave functions are computed and compared. They are furthermore tested on halo nuclei by calculations of momentum distributions and invariant mass spectra arising after fragmentation of fast ${}^6\text{He}$ and ${}^{11}\text{Li}$ in collisions with light targets. The prescriptions are very accurate and the available measured quantities are remarkably well reproduced when final state interactions are included.

PACS: 25.60.-t, 21.45.+v, 21.60.Gx

I. INTRODUCTION

Three-body models are useful to describe the relative wave function of three particles when their intrinsic structure remains unchanged [1–3]. The intrinsic and the relative degrees of freedom are then assumed to be completely decoupled. However, when the particles themselves are composite structures (clusters) and contain identical fermions this assumption violates the Pauli principle related to fermions distributed in different clusters. This violation typically leads to unphysical deeply bound two-cluster states. In the two-body problem this violation can be easily cured by removing this unphysical state from the active space available for the system.

In the three-cluster problem most of the usual approaches to include the Pauli principle basically fall into two categories: i) to project out the undesired overlap of the three-body wave function with the Pauli forbidden two-body state [4–6] and ii) to modify the two-body interaction in such a way that the unphysical bound cluster-cluster state is avoided, provided the low energy scattering properties [7] or the phase shifts [8,9] remain unchanged. The prescriptions basically amount to either excluding occupation of Pauli forbidden two-body states in the three-body wave function or excluding the a priori appearance of such undesired states. The two prescriptions give somewhat different results and it is not yet clear which one is preferable. The projection technique, although seems to be more straightforward, is in practice technically more difficult.

The problem of treating the intercluster Pauli principle again attracted attention in investigations of the structure of the three-body halo nuclei [2] where most of the information is obtained by studying momentum distributions of fragments of these nuclei in fast collisions with light targets. Originally these momentum distributions were expected to reveal the structure of the initial three-body wave function [10]. This is still true although more elaborate analyses are required. The correct account for the two-body interaction between fragments in the final state turned out to be essential when low lying resonances are present [11,12].

The purpose of the present paper is twofold. First we describe how the projecting out technique can be easily incorporated in the adiabatic hyperspherical expansion of the Faddeev equations in coordinate space [13]. This method to solve the Faddeev equations has already been used in several investigations of halo nuclei [3,14,15].

Secondly we investigate how the differences in the prescriptions are reflected in the momentum distributions of fragments from the break-up reactions of three-body halos. This question is important for an unambiguous interpretation of the wealth of experimental data on three-body halos like ${}^6\text{He}$ (${}^4\text{He}+n+n$) and ${}^{11}\text{Li}$ (${}^9\text{Li}+n+n$).

After the introduction we shall in section 2 describe the method and compare potentials and wave functions for two different prescriptions. In section 3 we use these wave functions in computations of momentum distributions in nuclear break-up reactions of three-body halo nuclei. Finally in section 4 we give a brief summary and the conclusions.

II. THREE-CLUSTER PROBLEM WITH PAULI FORBIDDEN TWO-CLUSTER STATES

Adiabatic hyperspherical expansion of the Faddeev equations. We shall use the hyperspherical coordinates $(\rho, \alpha, \Omega_x, \Omega_y)$ defined in refs. [2,3]. The volume element is given by $\rho^5 d\Omega d\rho$, where $d\Omega = \sin^2 \alpha \cos^2 \alpha d\alpha d\Omega_x d\Omega_y$. The

total wave function Ψ_{JM} of the three-body system (with total spin J and projection M) is written as a sum of three components, which in turn for each hyperradius ρ are expanded in a complete set of generalized angular functions $\Phi_n^{(i)}(\rho, \Omega_i)$

$$\Psi_{JM} = \frac{1}{\rho^{5/2}} \sum_n f_n(\rho) \sum_{i=1}^3 \Phi_n^{(i)}(\rho, \Omega_i), \quad (1)$$

where $\rho^{-5/2}$ is related to the volume element.

These wave functions satisfy the angular part of the three Faddeev equations:

$$\frac{\hbar^2}{2m} \frac{1}{\rho^2} \hat{\Lambda}^2 \Phi_n^{(i)} + V_{jk}(\Phi_n^{(i)} + \Phi_{nJM}^{(j)} + \Phi_n^{(k)}) \equiv \frac{\hbar^2}{2m} \frac{1}{\rho^2} \lambda_n(\rho) \Phi_n^{(i)}, \quad (2)$$

where $\{i, j, k\}$ is a cyclic permutation of $\{1, 2, 3\}$, m is an arbitrary normalization mass, and $\hat{\Lambda}^2$ is the ρ -independent part of the kinetic energy operator. The analytic expressions for $\hat{\Lambda}^2$ and the kinetic energy operator can for instance be found in [3].

The radial expansion coefficients $f_n(\rho)$ are obtained from a coupled set of ‘‘radial’’ differential equations [3], i.e.

$$\left(-\frac{d^2}{d\rho^2} - \frac{2mE}{\hbar^2} + \frac{1}{\rho^2} \left(\lambda_n(\rho) - Q_{nn} + \frac{15}{4} \right) \right) f_n(\rho) = \sum_{n' \neq n} \left(2P_{nn'} \frac{d}{d\rho} + Q_{nn'} \right) f_{n'}(\rho), \quad (3)$$

where the functions P and Q are defined as angular integrals:

$$P_{nn'}(\rho) \equiv \sum_{i,j=1}^3 \int d\Omega \Phi_n^{(i)*}(\rho, \Omega) \frac{\partial}{\partial \rho} \Phi_{n'}^{(j)}(\rho, \Omega), \quad (4)$$

$$Q_{nn'}(\rho) \equiv \sum_{i,j=1}^3 \int d\Omega \Phi_n^{(i)*}(\rho, \Omega) \frac{\partial^2}{\partial \rho^2} \Phi_{n'}^{(j)}(\rho, \Omega). \quad (5)$$

The radial equations in eq.(3) reveal that $\hbar^2(\lambda_n(\rho) - Q_{nn} + \frac{15}{4})/(2m\rho^2)$ is the diagonal part of the effective radial potential. Its behavior is decisive for the properties of the three-body system. The λ -spectrum at both $\rho = 0$ and $\rho = \infty$ is identical to the hyperspherical spectrum. In addition, for every bound two-body state, there exists one λ -value which bends over and diverges parabolically as function of ρ for $\rho \rightarrow \infty$, see [14]. Such a level corresponds at large distances to the three-body structure where the two-body subsystem is in the corresponding bound state, whereas the third particle is far away.

Treatment of the Pauli principle. The first prescription is a two-body potential without Pauli forbidden states but with the same low energy properties as the original deep two-body potential with the forbidden state. This corresponds to the use of an additional Pauli repulsion. We have discarded the apparently rigorous procedure of constructing the phase equivalent potential from the original two-body potential. The reasons are that the original interaction in any case appears in the form of an effective (mean) potential adjusted to reproduce specific measured quantities. Furthermore, the binding energy of the three-body system must be accurately reproduced to provide the correct structure. An additional fine tuning is therefore almost inevitable. The strictly phase equivalent potential is substantially more difficult to obtain and use. Under these circumstances we prefer to take the pragmatic approach and construct phenomenological potentials adjusted to have specifically chosen crucial properties.

The second prescription is a unique feature of the adiabatical expansion method. Since in this method each of the two-body bound states gives rise to a separate diverging λ -value, the prescription is simply to omit the λ -values corresponding to the Pauli forbidden two-body bound states from the expansion (1). Then all the Pauli forbidden states are automatically excluded in the three-body wave functions.

III. TWO-BODY POTENTIALS

We shall consider the two halo nuclei ${}^6\text{He}$ and ${}^{11}\text{Li}$, both approximated as three-body systems consisting of a core (${}^4\text{He}$ and ${}^9\text{Li}$) surrounded by two valence neutrons. This approximation works remarkably well for these systems and

furthermore due to relatively weak binding of the systems only the low energy parameters of the two-body potentials are essential for the structure of the systems [2]. As the core is inert in our approximation it is sufficient for our purpose to assume zero spin of the core for ^{11}Li .

In both cases the lowest neutron s-states in the core are filled. Therefore to conform with the Pauli principle the halo neutron should be prevented from occupying the lowest neutron-core s-state. We achieve this goal by use of two different neutron-core potentials with the same low energy properties. One of the potentials will have a Pauli forbidden bound state the other will not. This Pauli forbidden state will be consequently removed from the active space.

Neutron-neutron potential. As indicated in [2] and proved by our test runs the particular radial shape of the $n-n$ interaction is not important for ^6He and ^{11}Li ground state properties as long as the low energy $n-n$ scattering parameters are correct. We therefore use a simple potential similar to the one in [15] which reproduces the experimental s- and p-wave scattering lengths and effective ranges. It contains central, spin-orbit ($\mathbf{L} \cdot \mathbf{S}$), tensor (S_{12}) and spin-spin ($\mathbf{s}_1 \cdot \mathbf{s}_2$) interactions and is explicitly given as

$$\begin{aligned} V_{nn}(r) = & 37.05 \exp(-(r/1.31)^2) - 7.38 \exp(-(r/1.84)^2) \\ & - 23.77 \exp(-(r/1.45)^2) \mathbf{L} \cdot \mathbf{S} + 7.16 \exp(-(r/2.43)^2) S_{12} \\ & + (49.40 \exp(-(r/1.31)^2) + 29.53 \exp(-(r/1.84)^2)) \mathbf{s}_1 \cdot \mathbf{s}_2, \end{aligned} \quad (6)$$

where the strengths are in MeV and ranges in fm. Its scattering lengths¹ a and effective ranges r_e are (in fm) $a(^1S_0)=18.45$, $r_e(^1S_0)=2.83$, $a(^3P_0)=3.38$, $r_e(^3P_0)=1.10$, $a(^3P_1)=-2.02$, $r_e(^3P_1)=-2.94$, $a(^3P_2)=0.31$, $r_e(^3P_2)=18.73$.

Neutron- ^4He potential. For ^6He the low energy properties of the neutron-core subsystem in the s- and p-waves are rather well known and reflected in an s-wave scattering length of $a_s = -3.07 \pm 0.02$ fm and two resonance energies E and widths Γ of $E(p_{3/2}) = 0.77$ MeV, $\Gamma(p_{3/2}) = 0.64$ MeV and $E(p_{1/2}) \approx 1.97$ MeV, $\Gamma(p_{1/2}) \approx 5.22$ MeV, see [16]. The $p_{1/2}$ - $p_{3/2}$ splitting demands a spin-orbit force or equivalently (with the same range of the interactions) different strengths in the $p_{1/2}$ and $p_{3/2}$ channels. The negative s-wave scattering length can be reproduced by a repulsive potential or by an attractive potential with a bound state which in this case is the Pauli forbidden state occupied by the core neutrons.

We introduce central l-dependent and spin-orbit components in the potential with a gaussian shape $S \exp(-r^2/b^2)$. The range was chosen to be $b = 2.33$ fm for all components (similar to [2]) except for the repulsive s-wave where the range b was changed to 3.34 fm in order to reproduce the same effective range as for attractive potential. The strength parameters are then defined by the fit to the specified scattering length and positions of the resonances.

The p-wave strengths are $S(p_{1/2}) = -48.675$ MeV and $S(p_{3/2}) = -53.175$ MeV (or, equivalently, the central p-wave strength of -51.675 MeV and the spin-orbit strength of -3.00 MeV) which provide the p-wave resonances $E(p_{1/2}) = 1.94$ MeV, $\Gamma(p_{1/2}) = 4.0$ MeV and $E(p_{3/2}) = 0.77$ MeV, $\Gamma(p_{3/2}) = 0.73$ MeV. These parameters are the same for both repulsive and attractive s-wave potential.

The s-wave strength for the attractive potential (further referred to as ‘‘attractive’’) is $S(s_{1/2}) = -39.2$ MeV ($r_e=1.41$ fm and $a = -3.07$ fm, one Pauli forbidden bound state). Without additional fit these s- and p-wave potentials provide the binding energy $B(^6\text{He})=1.0$ MeV and r.m.s. radius $R(^6\text{He})=2.45$ fm, which is close to experimental data $B(^6\text{He})=0.97 \pm 0.04$ MeV and $R(^6\text{He})=2.57 \pm 0.10$ fm.

The repulsive s-wave potential which reproduces the experimental scattering length and the same effective range as the attractive potential slightly underbinds ^6He (by approximately 200 keV). Such underbinding for repulsive potentials is not unusual for ^6He . To alleviate this problem people normally increase the range of all potentials by a few per cent [2]. However this procedure shifts the positions of the p-resonances from their experimental values. As we shall see below these positions are extremely important for the momentum distributions. We therefore leave the p-waves unchanged and instead reduce slightly the repulsion in the s-wave.

The resulting potential is further referred to as ‘‘repulsive’’ and has the s-wave range and strength $b = 3.34$ fm, $S(s_{1/2}) = 9.70$ MeV, ($a = -2.58$ fm, $r_e = 0.67$ fm) which leads to the binding energy $B(^6\text{He})=1.0$ MeV and r.m.s. radius $R(^6\text{He})=2.50$ fm.

Neutron- ^9Li potential. For ^{11}Li the low energy neutron-core data are less known, although evidence is accumulating for a low lying virtual s-state at $E(s) \approx 0.15 \pm 0.15$ MeV and the lowest p-resonance at $E(p) \approx 0.6 \pm 0.2$ MeV, see [17–20]. The Pauli forbidden states are in this case both the lowest s-state and the $p_{3/2}$ -state. For simplicity the latter is in the calculations placed at high positive energy and thereby removed from the active space by a large inverse

¹our sign convention is $k^{2l+1} \cot(\delta) \xrightarrow{k \rightarrow 0} 1/a + r_e k^2/2$

spin-orbit potential [15]. For the s-waves we use a shallow potential without bound state and a deep potential with a Pauli forbidden state.

The radial shapes of the neutron-core interactions are also assumed to be gaussians, i.e. $S\exp(-r^2/b^2)$ with $b = 2.55$ fm [7] except for the deep s-wave potential with a bound state where we use $b = 1.49$ fm to maintain the same effective range as for the shallow potential.

We adopt further the usual assumption that the neutron-core interactions do not depend on the spin of the ${}^9\text{Li}$ -core. A more realistic study of ${}^{11}\text{Li}$ properties taking into account the spin of ${}^9\text{Li}$ has been made in [11,15].

Again the spin-orbit neutron-core potential effectively only gives different strengths for the two different p-waves. With the choice of range for the radial potentials there are only three strength parameters left each related to a resonance, a virtual state or a scattering length. The spin-orbit force is used to remove the Pauli forbidden $p_{3/2}$ -state from the active space. The two remaining strength parameters then determine the s- and $p_{1/2}$ -state as well as the binding energy of ${}^{11}\text{Li}$. One of them must be used to fine tune the binding energy B of the total three-body system $B({}^{11}\text{Li}) = 0.295 \pm 0.035$ MeV. With correct binding energy the root mean square radius is then always reproduced within the experimental uncertainty, which is $R({}^{11}\text{Li}) = 3.1 \pm 0.3$ fm.

The potential with a bound Pauli forbidden s-state (further referred to as “deep”) has the parameters $b = 1.49$ fm for the s-wave and $b = 2.55$ fm for p-waves, $S(s_{1/2}) = -176.608$ MeV (one bound state, $a=8.738$ fm, virtual level at 0.20 MeV), $S(p_{3/2}) = 9.55$ MeV ($E(p_{3/2})$ is high and uninteresting) and $S(p_{1/2}) = -38.34$ MeV ($E(p_{1/2}) = 0.77$ MeV, $\Gamma(p_{1/2}) = 0.89$ MeV). The binding energy and root mean square radius is then computed to be $B({}^{11}\text{Li})=0.30$ MeV and $R({}^{11}\text{Li})=3.34$ fm.

The shallow potential without bound states but with the same low energy properties as the deep potential overbinds ${}^{11}\text{Li}$ by some 180 keV. In contrast to ${}^6\text{He}$ the dominating component is now the s-wave in the neutron-core subsystem. Therefore to fine tune the binding energy we modify now the p-wave potential namely the position of the $p_{1/2}$ resonance while keeping the other properties unmodified.

The fine tuned potentials without a bound state (further referred to as “shallow”) has the parameters $b = 2.55$ fm, $S(s_{1/2}) = -7.14$ MeV (no bound state, $a=8.738$ fm, virtual level at 0.20 MeV), $S(p_{3/2}) = 9.55$ MeV ($E(p_{3/2})$ is high) and $S(p_{1/2}) = -35.45$ MeV ($E(p_{1/2}) = 1.7$ MeV, $\Gamma(p_{1/2}) = 4.2$ MeV). The binding energy and root mean square radius is now computed to be $B({}^{11}\text{Li})= 0.30$ MeV and $R({}^{11}\text{Li})= 3.35$ fm.

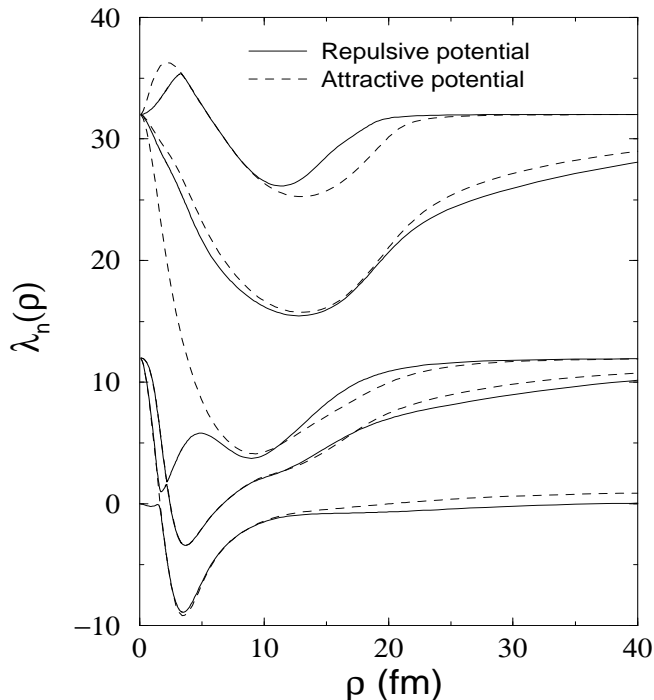


FIG. 1. Angular eigenvalue spectra λ_n as function of ρ for ${}^6\text{He}$ for the repulsive and attractive neutron- ${}^4\text{He}$ potentials described in the text. The lowest λ for the attractive potential originating from zero and corresponding to the Pauli forbidden state is removed.

IV. EFFECTIVE THREE-BODY ADIABATIC POTENTIALS

⁶He. The effective radial potential in eq.(3) is the crucial quantity which in turn mainly is determined by the λ -spectrum. The two prescriptions for dealing with the Pauli principle lead to different spectra as seen in fig. 1 for ⁶He. The purely repulsive neutron-core s-wave potential (solid curves) results in the steep increase of the lowest λ -value at small ρ . The increase is quickly interrupted by two (avoided) crossings involving the next two λ -values, which in contrast are moving steeply down due to the strong p-wave attraction leading to a low lying p-resonance in ⁵He (see the parameters given in the previous section). They therefore must contain a substantial amount of p-wave and the related components must be dominating in the wave function which accordingly also has about 87% p-wave and 13% s-wave in the relative neutron-core system. The curves eventually return back recovering the hyperspherical spectrum for $\rho = \infty$. This occurs without (avoided) level crossings. The interaction between crossing levels is vanishing or small indicating different symmetries of these levels. The related almost preserved quantum numbers are the neutron-core relative angular momenta $l_x = 0$ and 1 corresponding to states originating from zero and from 12. The two levels originating from 32 are apparently at small ρ dominated respectively by s- and p-wave components. At larger ρ the highest λ bends over due to p-wave admixture and the related strong attraction.

The λ -spectrum for the other potential with sufficient attraction in the neutron-core s-wave to support one bound s-state is also shown as the dashed curves in fig. 1. The lowest λ -value is not shown in the figure. It is mainly s-waves in the neutron-core subsystem and decreases at small ρ and diverges parabolically for $\rho \rightarrow \infty$ as clear signals of strong attraction and a resulting bound state. All states built on this (not plotted) level are Pauli forbidden and the level is therefore excluded in the following calculations. The two next λ -values on the other hand remain almost unchanged (apart from the avoided crossings) indicating a dominating p-wave content (about 93%) in the relative neutron-core subsystem. This behavior is consistent with an almost unchanged energy of the lowest lying p-resonance in the two-body subsystem. As the lowest lying levels dominate the wave function the behavior of these effective potentials also guarantee an almost identical wavefunction in the two approaches. Also the two highest λ -values remain essentially unchanged. The third λ -value start out as an s-wave as seen from the strong decrease. At larger distances it is then replacing the s-wave originating from zero (crossing two times) from the purely repulsive potential.

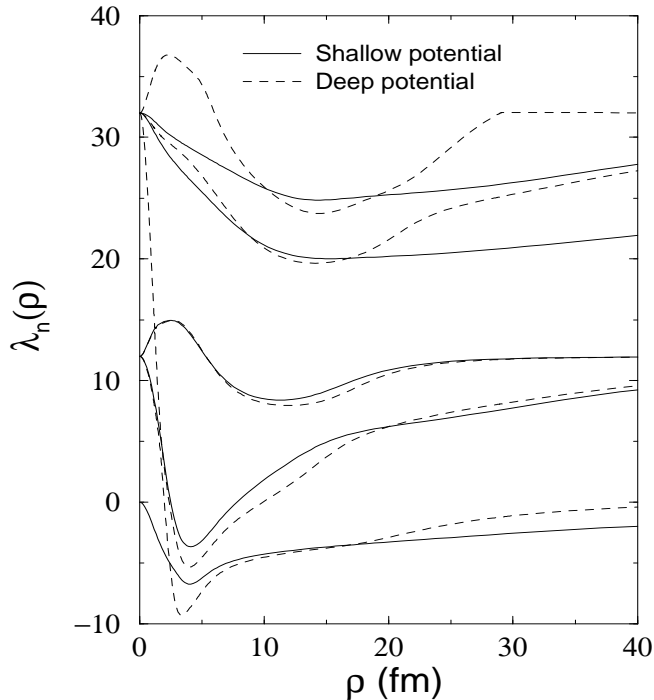


FIG. 2. Angular eigenvalue spectra λ_n as function of ρ for ¹¹Li for the shallow and deep neutron-⁹Li potentials described in the text. The lowest λ for the deep potential originating from zero and corresponding to the Pauli forbidden state is removed.

¹¹Li. For ¹¹Li the low lying s-state of ¹⁰Li results in a structure where the dominating neutron-core relative configuration is an s-state. This is rather different from ⁶He where the predominant neutron-core relative configurations were p-states. The λ -spectra for the two potentials corresponding to the different prescriptions are shown in fig. 2. The shallow attractive potential without a bound s-state (solid curves) results in a rather slowly changing lowest λ -value which contains essentially only neutron-core s-waves. This would by far carry the largest probability in the resulting wave function. The two highest λ -values are also smooth functions of ρ while the second level steeply decreases at small ρ indicating attraction in the corresponding partial wave.

The other potential, which has a Pauli forbidden bound neutron-core s-state, has much stronger s-wave attraction and a λ -spectrum, see dashed curves fig. 2, with a fast moving level originating from 32. This level responds to the large s-wave attraction and crosses quickly the two levels originating from 12 before replacing the lowest level from the shallow potential. This level will dominate the configuration of the radial wave function. The lowest λ -value originating from zero is not plotted and also omitted in the following calculations. It decreases at small ρ and diverges parabolically at large ρ . The four remaining levels all have similarly behaving counter parts in the other spectrum. Again we see the (avoided) crossings indicating almost conserved quantum numbers on the levels. As before they can be traced back to the neutron-core relative angular momentum $l_x = 0$ and 1.

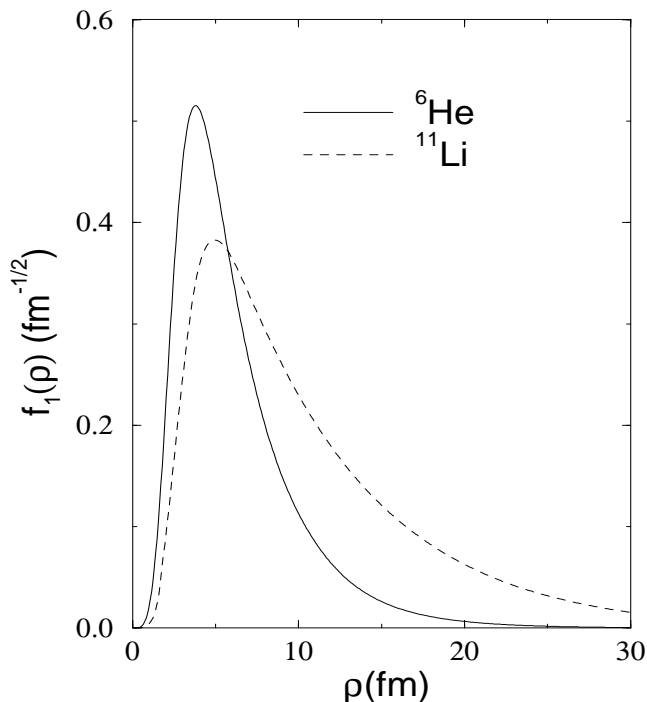


FIG. 3. The radial wave functions for ⁶He (solid curve) and ¹¹Li (dashed curve) corresponding to the lowest dominating λ -values for the potentials with Pauli forbidden bound states.

Radial functions. The radial wave function corresponding to the lowest λ is shown in fig. 3 for the two nuclei. This component is responsible for more than 90% of the wave function. Only the result of one of the prescriptions is shown for each case, since the curves would be difficult to distinguish especially at larger distances where they are very close. This is closely related to the fact that the binding energies and radii are the same in both prescriptions. The wave function is spatially more extended for ¹¹Li than for ⁶He, again reflecting the difference in binding energy.

V. MOMENTUM DISTRIBUTIONS

The momentum distributions after fragmentation of halo nuclei is a very direct way of gaining detailed information about the relative wave function of these nuclei. It was originally expected simply to provide the Fourier transform, but more complicated and detailed analyses are needed. Such computations are fortunately available at this moment

and we shall exploit this avenue to test our prescriptions.

The sudden approximation. We consider a process where a high-energy three-body halo projectile instantaneously loses one of the particles without disturbing the remaining two. We also assume a light target and we shall therefore neglect the Coulomb dissociation process, which then only contributes marginally.

We work in the center of mass system of the three-body projectile and denote by \mathbf{k}_y and \mathbf{k}_x the total and relative momentum of the two remaining particles in the final state. The transition matrix of the reaction in the sudden approximation is then given by

$$M_{s_x\sigma_x s_y\sigma_y}^{JM}(\mathbf{k}_y, \mathbf{k}_x) \propto \langle e^{i\mathbf{k}_y \cdot \mathbf{y}} \chi_{s_y\sigma_y} w_{s_x\sigma_x}(\mathbf{k}_x, \mathbf{x}) | \Psi_{JM} \rangle, \quad (7)$$

where Ψ_{JM} is the three-body wave function and $w_{s_x\sigma_x}$ is the final state *distorted* two-body wave function [11] corresponding to the two remaining particles with the distance \mathbf{x} , total spin and projection equal to s_x and σ_x . The distance between the center of mass of the two-body system and the removed particle is \mathbf{y} and $\chi_{s_y\sigma_y}$ is the spin wave function of the third particle where s_y and σ_y are the related total spin and projection.

The cross section or momentum distribution is now obtained by squaring the transition matrix and subsequently averaging over initial states and summing over final states:

$$\frac{d^6\sigma}{d\mathbf{k}_x d\mathbf{k}_y} \propto \sum_M \sum_{s_x\sigma_x s_y\sigma_y} |M_{s_x\sigma_x s_y\sigma_y}^{JM}(\mathbf{k}_x, \mathbf{k}_y)|^2. \quad (8)$$

Using the momentum $\mathbf{p}(= a\mathbf{k}_x + b\mathbf{k}_y)$ of one of the particles relative to the center of mass of the projectile as the variable instead of \mathbf{k}_x , we obtain the relation

$$\frac{d^6\sigma}{d\mathbf{p}d\mathbf{k}_y} = \frac{1}{a^3} \frac{d^6\sigma}{d\mathbf{k}_x d\mathbf{k}_y} \propto \frac{1}{a^3} \sum_M \sum_{s_x\sigma_x s_y\sigma_y} |M_{s_x\sigma_x s_y\sigma_y}^{JM}(\mathbf{k}_x, \mathbf{k}_y)|^2, \quad (9)$$

where a^3 arises from the Jacobi determinant for the transformation. The differential cross section in eq.(9) should be integrated over all unobserved variables, i.e. \mathbf{k}_y and some of the components of \mathbf{p} . Note that we have not specified any coordinate system, and the axis \mathbf{x} , \mathbf{y} , and \mathbf{z} are therefore completely arbitrary. Thus, in our approximation the longitudinal and transverse momentum distributions are identical.

After neutron removal fragmentation reactions is usual to define the invariant mass $E_{\text{core+n}}$ as

$$E_{\text{core+n}} = ((E_{\text{core}} + E_n)^2 + c^2(\mathbf{p}_{\text{core}} + \mathbf{p}_n)^2)^{1/2} - (M_{\text{core}} + M_n)c^2, \quad (10)$$

where $E_{\text{core,n}}$, $\mathbf{p}_{\text{core,n}}$, and $M_{\text{core,n}}$ denote the energy, three-momentum, and rest mass of the core and the neutron, respectively.

Computing the invariant mass in the frame of the two-body system after the fragmentation ($\mathbf{p}_{\text{core}} + \mathbf{p}_n = 0$) we have

$$p_{\text{core}}^2 c^2 = p_n^2 c^2 = \frac{1}{m} \frac{M_{\text{core}} M_n}{M_{\text{core}} + M_n} k_x^2 c^2 = E_{\text{core}}^2 - M_{\text{core}}^2 c^4 = E_n^2 - M_n^2 c^4, \quad (11)$$

and

$$dE_{\text{core+n}} = dE_{\text{core}} + dE_n = \frac{E_{\text{core}} + E_n}{E_{\text{core}} E_n} \frac{M_{\text{core}} M_n}{m(M_{\text{core}} + M_n)} k_x dk_x \quad (12)$$

The invariant mass spectrum is then defined

$$\frac{d\sigma}{dE_{\text{core+n}}} = \frac{E_{\text{core}} E_n}{E_{\text{core}} + E_n} \frac{m(M_{\text{core}} + M_n)}{M_{\text{core}} M_n} \frac{1}{k_x} \frac{d\sigma}{dk_x} \quad (13)$$

where $d\sigma/dk_x$ is obtained from eq.(8) after integrating over the unobserved quantities.

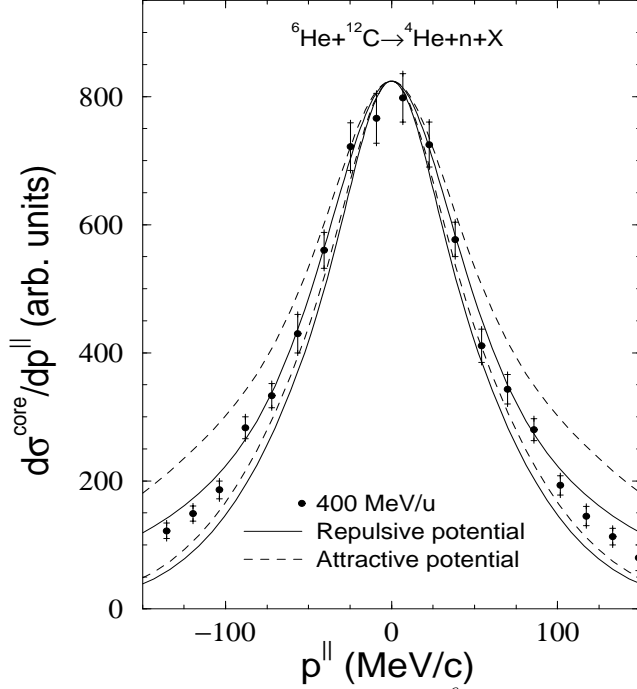


FIG. 4. Longitudinal core momentum distributions for a ${}^6\text{He}$ neutron removal reaction computed for both the purely repulsive potential (solid curve) and the attractive potential with one bound s-state (dashed curve) defined in fig. 1. The broadest distributions correspond to the neglect of final state interaction. The experimental points for fast ${}^6\text{He}$ (400 MeV/u) colliding with a carbon target are from [21], and correspond to the transverse core momentum distribution. The core momentum is referred to the center of mass system of the three-body projectile.

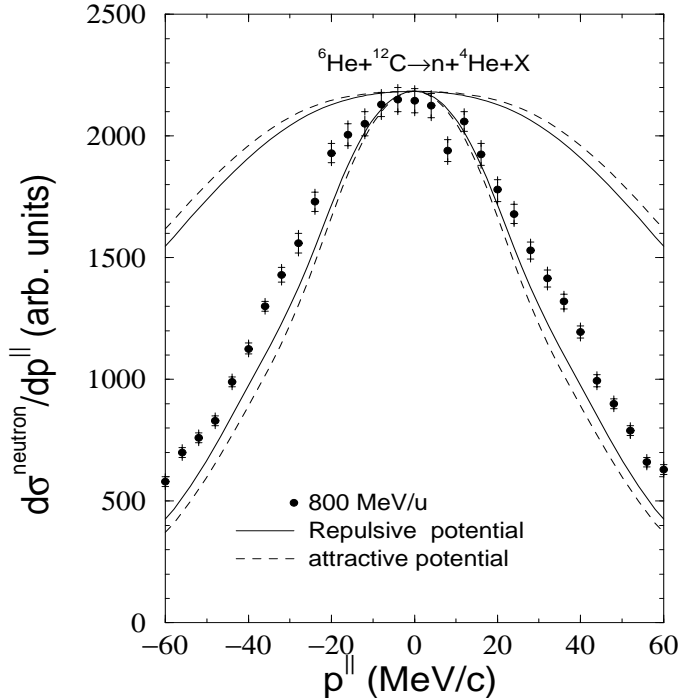


FIG. 5. Longitudinal neutron momentum distributions for a ${}^6\text{He}$ neutron removal reaction computed for both the repulsive potential (solid curve) and the attractive potential with one bound s-state (dashed curve) defined in the text. The broadest distributions correspond to the neglect of final state interaction. The experimental points for fast ${}^6\text{He}$ (800 MeV/u) colliding with a carbon target are from [23], and correspond to the transverse neutron momentum distribution. The neutron momentum is referred to the center of mass system of the three-body projectile.

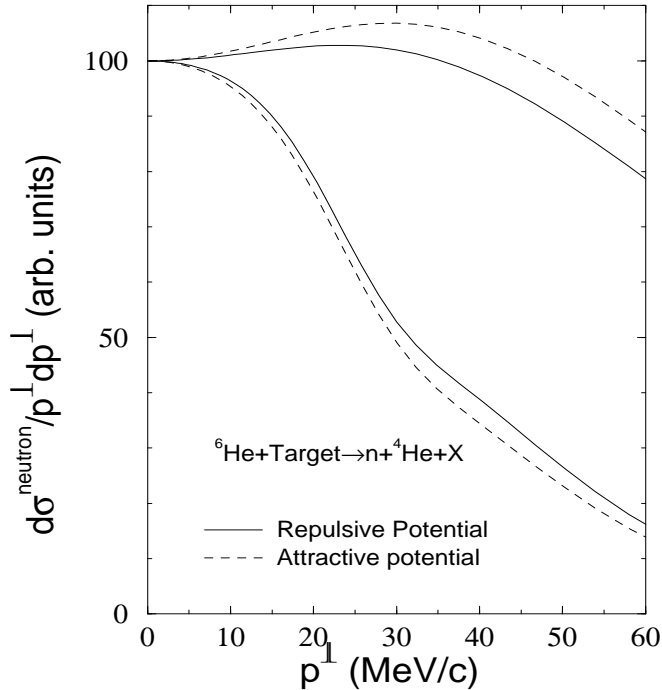


FIG. 6. Radial neutron momentum distributions for a ${}^6\text{He}$ neutron removal reaction computed for both the repulsive potential (solid curve) and the attractive potential with one bound s-state (dashed curve) defined in the text. The broadest distributions correspond to the neglect of final state interaction. The neutron momentum is referred to the center of mass system of the three-body projectile.

${}^6\text{He}$ fragmentation. In fig. 4 the computed longitudinal core momentum distribution after neutron removal in a fast nuclear break-up reaction of ${}^6\text{He}$ on a light target is shown. The results of the two prescriptions are exhibited both with and without inclusion of the final state interaction. As expected the effect of the final state interaction is visible but not extremely important even with this fairly light core. The results of the two prescriptions are very close when the final state interaction is included. When it is neglected the intrinsic differences in the wave functions obtained with the two different prescriptions to account for the Pauli principle produce a clear distinction. The difference is in the additional node of the forbidden state prescription compared to the reduced attraction prescription. The experimental data in fig. 4 are taken from [21], and correspond to the transverse core momentum distribution after fast ${}^6\text{He}$ fragmentation on a carbon target. The present model computations do not distinguish between directions, but the results are expected to be more appropriate for the longitudinal directions, which unfortunately are unavailable at this moment. However, the agreement with the measured results is still encouraging for several reasons. First, we have basically no free parameters. Second, the experimental transverse momentum distributions are expected to be broader than the longitudinal ones [22]. Third, no broadening due to neglected effects and experimental resolution is included in the computation.

In figs. 5 and 6 we show corresponding computed longitudinal and radial ($p^\perp = (p_x^2 + p_y^2)^{1/2}$) neutron momentum distributions for a neutron removal ${}^6\text{He}$ fragmentation reaction. Again the two prescriptions give very similar results when the final state interaction is included. In this case we obtain a very large influence of the final state interaction which reduce the full width at half maximum by a factor 2-3. Inclusion of the final state interaction is therefore necessary to obtain the observed agreement with the measured values. We want here to emphasize that the computed results are found in a consistent model where the same two-body potential is responsible for both the three-body structure of the initial halo state and the final state interaction after break-up. The experimental data in fig. 5 are obtained from [23], and correspond to the transverse neutron momentum distribution after ${}^6\text{He}$ fragmentation on a carbon target at 800 MeV/u. Again the computed curve is expected to compare more favourably with the experimental longitudinal neutron momentum distribution. However, these data are not presently available.

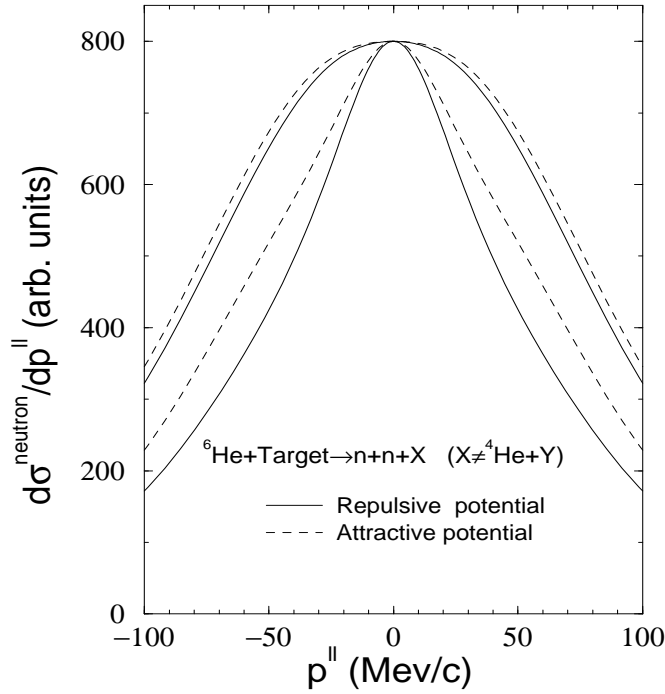


FIG. 7. Longitudinal neutron momentum distributions for a ${}^6\text{He}$ core break-up reaction computed for both the repulsive potential (solid curve) and the attractive potential with one bound s -state (dashed curve) defined in the text. The broadest distributions correspond to the neglect of final state interaction. The neutron momentum is referred to the center of mass system of the three-body projectile.

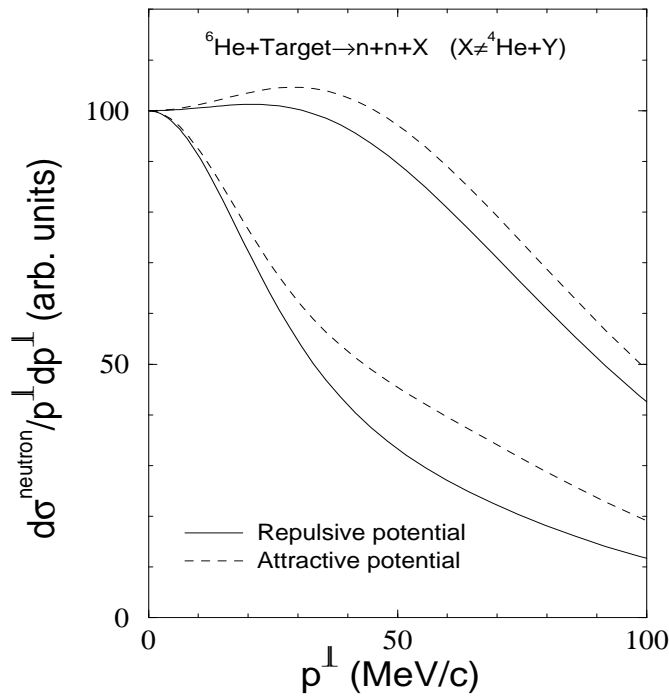


FIG. 8. Radial neutron momentum distributions for a ${}^6\text{He}$ core break-up reaction computed for both the repulsive potential (solid curve) and the attractive potential with one bound s -state (dashed curve) defined in the text. The broadest distributions correspond to the neglect of final state interaction. The neutron momentum is referred to the center of mass system of the three-body projectile.

Although measured values are not available we show in figs. 7 and 8 the computed longitudinal and radial neutron momentum distributions for core break-up reactions of ${}^6\text{He}$. In this case the core is violently removed, and the final neutron-neutron interaction is relevant. The two prescriptions again lead to similar results. The final state interaction can not be neglected due to the low lying virtual s-state in the neutron-neutron system.

Key quantities for a number of different cases are given in table I, where the ${}^6\text{He}$ binding energy and radius are kept at the measured values. For the case of the repulsive s-wave potential we have first considered two cases (first two rows of table I) where both the $p_{1/2}$ and the $p_{3/2}$ -resonance energies lie within the experimental values. In these two cases the computed scattering length for the s-wave is smaller than the experimental value of -3.07 . Increasing the absolute size of the computed s-wave scattering length (keeping fixed the energy of the lowest $p_{3/2}$ -resonance) reduces the energy of the $p_{1/2}$ -resonance (case 3 in the table). When the scattering length is equal to the experimental value the energy of the second p-resonance is below the experimental energy. Cases 4 to 6 in table I are analogous to cases 1 to 3, but with an s-wave repulsive potential giving a clearly worse agreement with the experimental s-wave scattering length. However the changes in the full width at half maximum of the momentum distributions, the p-wave content and root mean square radius, are very small, reflecting that the properties the s-wave interaction do not play an essential role in the structure of ${}^6\text{He}$.

For an attractive s-potential with one bound state (two last rows of table I) it is possible to reproduce both the experimental s-wave scattering length and the two p-wave resonance energies. For the two cases 7 and 8 shown in table I the variation of the energy of the $p_{1/2}$ -resonance only produces a change in the ${}^6\text{He}$ binding energy of about 70 keV, but in both cases consistent with a computed value of 1.0 MeV. The cases 1 and 7 correspond to the parameters given in section 3, and they are the two cases considered for ${}^6\text{He}$ in figs. 4, 5, 6, 7, and 8.

¹¹*Li fragmentation.* The interaction parameters for the schematic ¹¹Li computation, where the core spin is assumed to be zero, only provide the s- and $p_{1/2}$ -strengths for fine tuning. We already placed the $p_{3/2}$ -state at a very high energy and thereby removed it from the active space. In contrast to ${}^6\text{He}$ the dominating component is now an s-wave in the neutron-core subsystem. In table II we show the relevant quantities for three different computations. The first row corresponds to a computation with a shallow s-wave potential without bound states while the second and third rows correspond to computations with deep s-wave potentials with one bound state. The effective range and scattering length are the same in the three cases and the s-wave interaction places the lowest virtual s-state at 200 keV. Once the s-wave potential has been fixed the energy of the $p_{1/2}$ -resonance must then be around 1.7 MeV for the shallow potential case in order to fit the ¹¹Li binding energy. When the deep potential is used we consider two situations. First we keep the energy of the $p_{3/2}$ -resonance unchanged. Then the $p_{1/2}$ -energy is reduced to 0.8 MeV in order to recover the ¹¹Li binding energy. In the second case we force the $p_{1/2}$ -resonance energy to take the same value as for the shallow potential. The correct ¹¹Li binding energy is in this case obtained by reducing the energy of the $p_{3/2}$ -resonance. The cases 1 and 2 correspond to the parameters given in section 3 and they will be the two cases considered for ¹¹Li in the next figures (more elaborated and detailed computations for ¹¹Li fragmentation reactions may be found elsewhere, see [11]).

| case | $E(s_{1/2})$ (MeV) | a (fm) | $E(p_{1/2})$ (MeV) | $\Gamma(p_{1/2})$ (MeV) | Γ_c (MeV/c) | Γ_n (MeV/c) | p -content (%) | R (fm) |
|------|-----------------------|-------------|-----------------------|----------------------------|-----------------------|-----------------------|---------------------|-----------|
| 1 | 5.27 | -2.58 | 1.94 | 4.02 | 101.6 | 72.6 | 87.7 | 2.50 |
| 2 | 5.13 | -2.21 | 2.55 | 7.38 | 100.5 | 74.8 | 86.2 | 2.50 |
| 3 | 5.09 | -3.07 | 1.28 | 1.77 | 103.0 | 68.1 | 89.4 | 2.50 |
| 4 | 10.6 | -2.04 | 1.94 | 4.02 | 98.8 | 72.9 | 86.7 | 2.53 |
| 5 | 10.8 | -1.80 | 2.55 | 7.38 | 98.3 | 74.5 | 85.5 | 2.53 |
| 6 | 9.3 | -2.51 | 1.10 | 1.34 | 99.2 | 67.1 | 88.5 | 2.53 |
| 7 | 5.08 | -3.07 | 1.94 | 4.02 | 107.6 | 67.4 | 92.8 | 2.45 |
| 8 | 5.08 | -3.07 | 2.55 | 7.38 | 106.2 | 68.1 | 92.7 | 2.49 |

TABLE I. Key quantities for ${}^6\text{He}$ corresponding to various neutron-core interactions which are chosen as gaussians in each partial wave. The neutron-neutron interaction is given in Section 3. For the neutron- ${}^4\text{He}$ subsystem we give energies of the virtual $s_{1/2}$ -state, s-wave scattering lengths, energies and widths of the $p_{1/2}$ -resonance. The $p_{3/2}$ -resonance energy and width are in all cases 0.77 MeV and 0.73 MeV, respectively. The full width at half maximum for core and neutron momentum distributions is denoted Γ_c and Γ_n . We also give the probability for finding the neutron- ${}^4\text{He}$ subsystem in a p -wave in the three-body wave function of ${}^6\text{He}$. The remaining probability is found in s-waves. The total binding energy of the three-body system is in all cases equal to about 1.0 MeV and the root mean square radius is given in the last column. Cases 1-6 and 7-8 correspond to potentials without bound and with one bound s-state, respectively.

Looking at the root mean square radius we observe that it only varies between about 3.30 fm and 3.40 fm independently of the prescription and mainly sensitive to the amount of s-state in the neutron-core subsystem, see also [15]. The deep potential gives almost the same radius as the shallow potential. This is in contradiction with the large radii (≥ 3.50 fm) obtained in similar Faddeev calculations, where the lowest s-state is projected out [24]. These surprisingly large radii are hard to reconcile with the general asymptotic relation between binding energy and radius for weakly bound halo nuclei [3,14]. Incidentally a similarly large radius (3.55 ± 0.10 fm) is also obtained in recent Glauber analyses of the measured reaction cross section [25]. The reliability of such analyses still remains to be investigated.

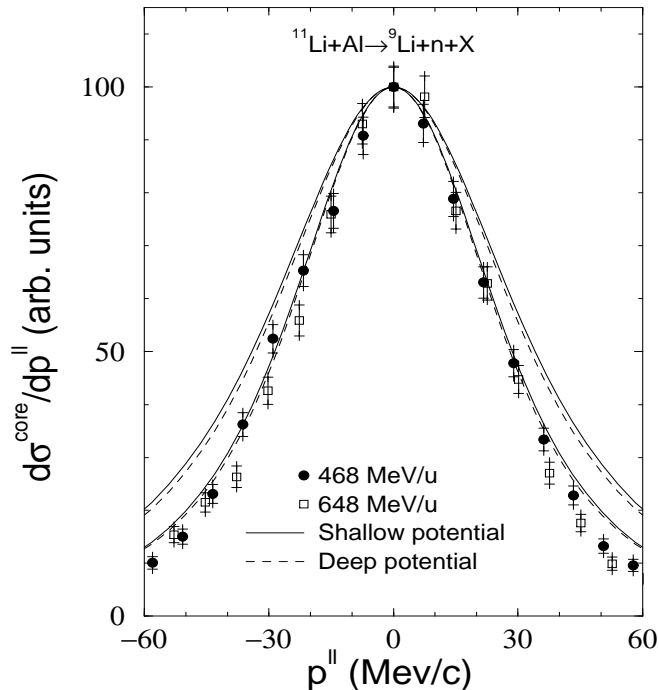


FIG. 9. Longitudinal core momentum distributions for a ^{11}Li neutron removal reaction computed for both the shallow potential (solid curve) and the deep potential with one bound s-state (dashed curve) defined in the text. The broadest distributions correspond to the neglect of final state interaction. The experimental points for fast ^{11}Li (468 MeV/u and 648 MeV/u) colliding with a aluminium target are from [26]. The core momentum is referred to the center of mass system of the three-body projectile.

| case | $E(s_{1/2})$ (MeV) | a (fm) | $E(p_{1/2})$ (MeV) | $\Gamma(p_{1/2})$ (MeV) | Γ_c (MeV/c) | Γ_n (MeV/c) | p -content (%) | R (fm) |
|------|-----------------------|-------------|-----------------------|----------------------------|-----------------------|-----------------------|---------------------|-----------|
| 1 | 0.200 | 8.738 | 1.68 | 4.16 | 57.6 | 34.8 | 17.3 | 3.34 |
| 2 | 0.200 | 8.738 | 0.77 | 0.89 | 56.1 | 38.2 | 21.0 | 3.35 |
| 3 | 0.200 | 8.738 | 1.68 | 4.16 | 55.6 | 35.6 | 15.6 | 3.37 |

TABLE II. Key quantities for ^{11}Li corresponding to various neutron-core interactions which are chosen as gaussians in each partial wave. The neutron-neutron interaction is given in section 3. For the neutron- ^9Li subsystem we give energies of the virtual $s_{1/2}$ -state, s-wave scattering lengths, energies and widths of the $p_{1/2}$ -resonance. The width and energy of the $p_{3/2}$ -resonance is unphysical and not included. The full width at half maximum for core and neutron momentum distributions is denoted Γ_c and Γ_n . We also give the probability for finding the neutron- ^{10}Li subsystem in a p -wave in the three-body wave function of ^{11}Li . The remaining probability is found in s-waves. The total binding energy of the three-body system is in all cases equal to about 0.30 MeV and the root mean square radius is given in the last column. Cases 2 and 3 correspond to potentials with one bound s-state.

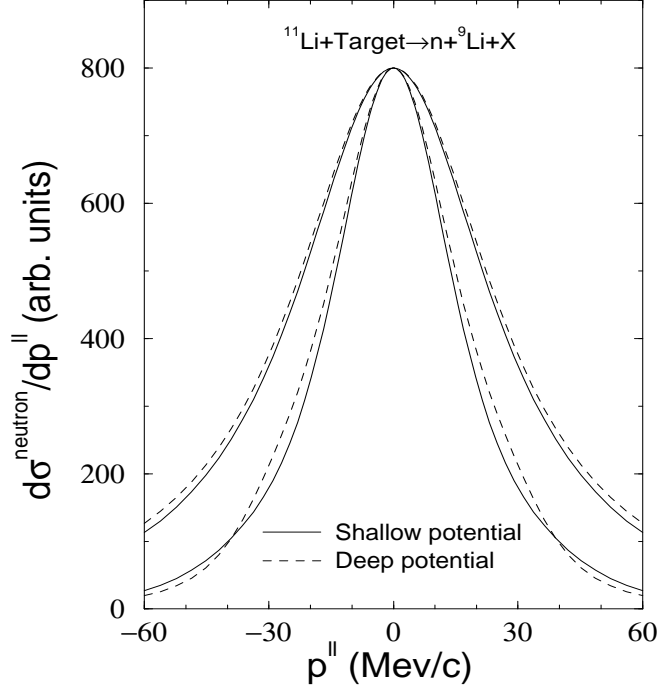


FIG. 10. Longitudinal neutron momentum distributions for a ^{11}Li neutron removal reaction computed for both the shallow potential (solid curve) and the deep potential with one bound s-state (dashed curve) defined in the text. The broadest distributions correspond to the neglect of final state interaction. The neutron momentum is referred to the center of mass system of the three-body projectile.

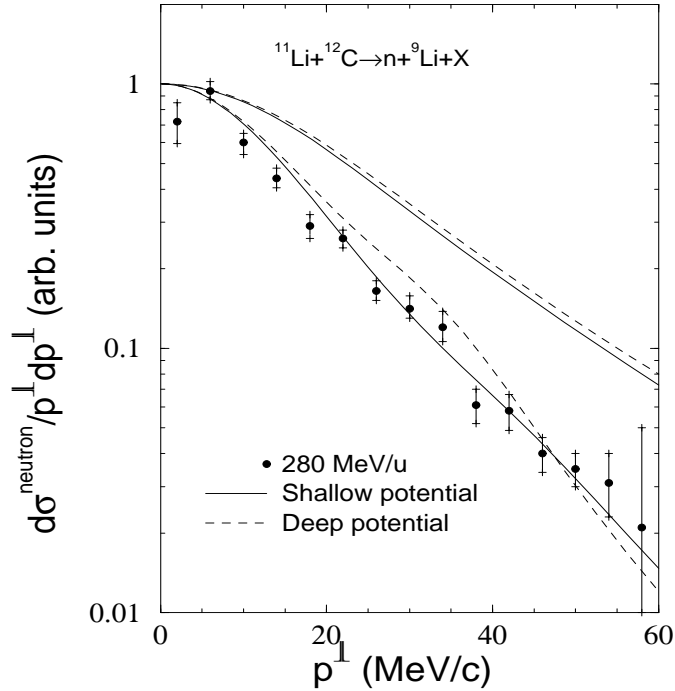


FIG. 11. Radial neutron momentum distributions for a ^{11}Li neutron removal reaction computed for both the shallow potential (solid curve) and the deep potential with one bound s-state (dashed curve) defined in the text. The broadest distributions correspond to the neglect of final state interaction. The experimental points for fast ^{11}Li (280 MeV/u) colliding with a carbon target are from [19]. The neutron momentum is referred to the center of mass system of the three-body projectile.

In fig. 9 we show the computed longitudinal core momentum distributions after neutron removal in a fast nuclear break-up reaction of ^{11}Li on a light target. We assume that the ^9Li -core has spin zero. The model is then without the proper spin couplings and the spin splitting of the neutron-core relative states [15]. Although simplified the model is still not far from being realistic. The two prescriptions again give very similar results and the effect of the final state interaction is now a little smaller than for ^6He due to the larger mass of the core nucleus. The experimental distributions are essentially reproduced, and correspond to a ^{11}Li fragmentation reaction on Al at 468 MeV/u and 648 MeV/u [26].

In figs. 10 and 11 we show computed longitudinal and radial ($p^\perp = (p_x^2 + p_y^2)^{1/2}$) neutron momentum distributions for a neutron removal reaction of ^{11}Li . The cases shown in the figure correspond to rows 1 and 2 of table II. The difference in energy of the $p_{1/2}$ resonance in the neutron-core subsystem produces the difference in the momentum distribution when the final state interaction is included. In fact the momentum distributions obtained in the third case of table II are almost indistinguishable from those obtained in the first case (the energy of the $p_{1/2}$ resonance is the same in these two cases). The final state interaction is then important due to the presence of low lying virtual s-states and p-resonances, and very sensitive to the energies of these low lying states.

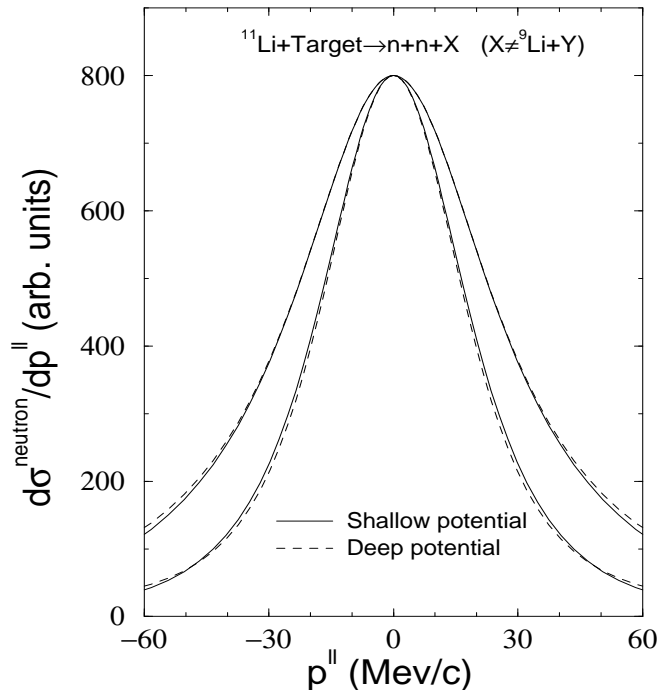


FIG. 12. Longitudinal neutron momentum distributions for a ^{11}Li core break-up reaction computed for both the shallow potential (solid curve) and the deep potential with one bound s-state (dashed curve) defined in the text. The broadest distributions correspond to the neglect of final state interaction. The neutron momentum is referred to the center of mass system of the three-body projectile.

For completeness we show in figs. 12 and 13 the longitudinal and radial neutron momentum distribution from a ^{11}Li core break-up reaction. We again observe an important effect produced by the inclusion of the final neutron-neutron interaction (the neutron-neutron interaction has a low lying virtual s-state), and an almost identical result for both the shallow and deep neutron- ^9Li s-wave potential. In figs. 11 and 13 the experimental data are fairly well reproduced, and correspond to a ^{11}Li fragmentation reaction at 280 MeV/u on a carbon target [19,27]

Invariant mass spectrum. Computing the invariant mass $E_{\text{core}+n}$ (eq.(10)) in the frame of the two-body system in the final state ($\mathbf{p}_{\text{core}} + \mathbf{p}_n = 0$) we can interpret $E_{\text{core}+n}$ as the kinetic energy of the neutron-core system in the final state:

$$E_{\text{core}+n} \approx \frac{p_{\text{core}}^2}{2\mu} = \frac{p_n^2}{2\mu} = \frac{k_x^2}{2m} \quad (14)$$

where μ and m are the reduced mass of the two-body system and the arbitrary normalization mass, respectively. The energy of a resonance is defined as the $k_x^2/2m$ value for which the cross section has a maximum. As a consequence the invariant mass spectrum (13) will show a peak at the $E_{\text{core}+n}$ energy equal to a resonance energy.

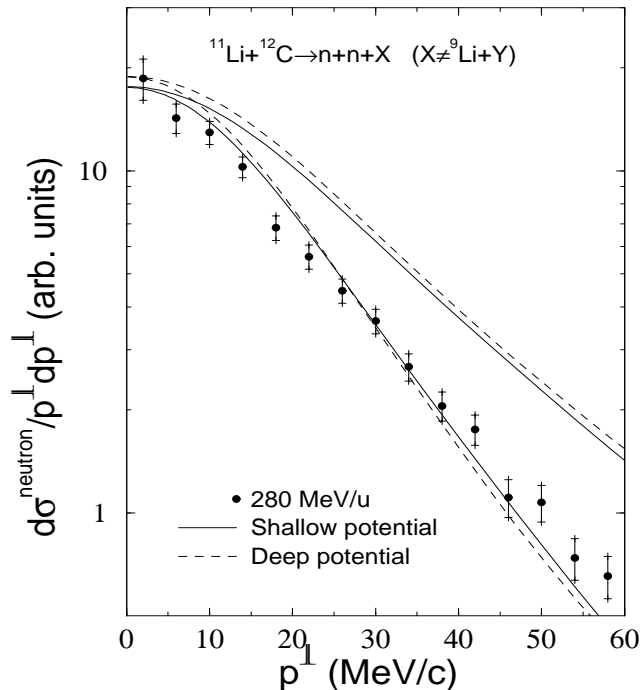


FIG. 13. Radial neutron momentum distributions for a ^{11}Li core break-up reaction computed for both the shallow potential (solid curve) and the deep potential with one bound s-state (dashed curve) defined in the text. The broadest distributions correspond to the neglect of final state interaction. The experimental points for fast ^{11}Li (280 MeV/u) colliding with a carbon target are from [27]. The neutron momentum is referred to the center of mass system of the three-body projectile.

In fig. 14 we show the invariant mass spectrum (13) from a ^6He neutron removal reaction. The cases with repulsive s-potential (solid line) and attractive s-potential with a Pauli forbidden state (short-dashed line) are shown. The parameters correspond to cases 1 and 7 in table I, respectively. As seen from the figure, both curves are very similar, and show a peak around $E_{\text{core}+n} = 0.8$ MeV, that corresponds to the energy of the $p_{3/2}$ resonance. Another p-resonance is present at 2 MeV in ^5He . However its width is much larger than before, and therefore its effect on the spectrum is much more spreaded out. To illustrate how the invariant mass spectrum is sensitive to the resonance energies we also show the case where the neutron- ^4He potential introduced in ref. [2] is used (long-dashed line). The suggested increase by 3% of the range of the neutron- ^4He potential makes the energy of the $p_{3/2}$ resonance too small (around 0.3 MeV), giving rise to the pronounced peak in the invariant mass spectrum at that energy. The different height of the curves in fig. 14 comes from the fact that all the three curves are normalized to 1.

In fig. 15 we show the same spectrum as in fig. 14 from a neutron removal ^{11}Li reaction. The cases of the shallow and deep potentials are shown (cases 1 and 2 in table II). The difference between these two cases comes from the different energy of the lowest p-resonance.

For the deep potential (dashed line) the $p_{1/2}$ resonance is at 0.77 MeV, creating a clear shoulder in the curve at that energy. Note that the contribution to the wave function from the p-wave (21% probability) is given directly by the schematic model. It is determined by the energies of the virtual $s_{1/2}$ state and the $p_{1/2}$ resonance together with the requirement of fitting the binding energy and radius of ^{11}Li . Therefore the shoulder in the distribution is less pronounced than in calculations where the p-wave content is chosen to be higher, for instance in [28], where a rather arbitrary 50% contribution for the p-waves is chosen. For the shallow potential (solid curve) the large width of the resonance at 1.7 MeV broadens the corresponding peak at that energy and it disappears completely. For both the deep and the shallow potential the lowest peak comes from the low lying virtual s-state in ^{10}Li . However in this case the position of the peak is not directly related to the energy of the virtual state. A virtual state produces an increase

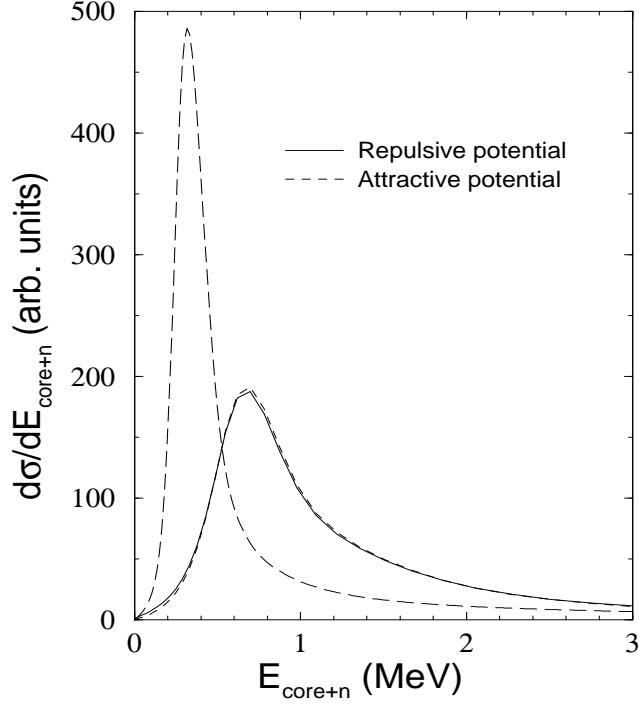


FIG. 14. The invariant mass spectrum for a ${}^6\text{He}$ neutron removal reaction computed for both the repulsive potential (solid curve) and the attractive potential with one bound s-state (short-dashed curve) defined in the text. The case of the potential introduced in ref. [2] (with an increase of 3% of the range of the potential) is also shown (long-dashed line).

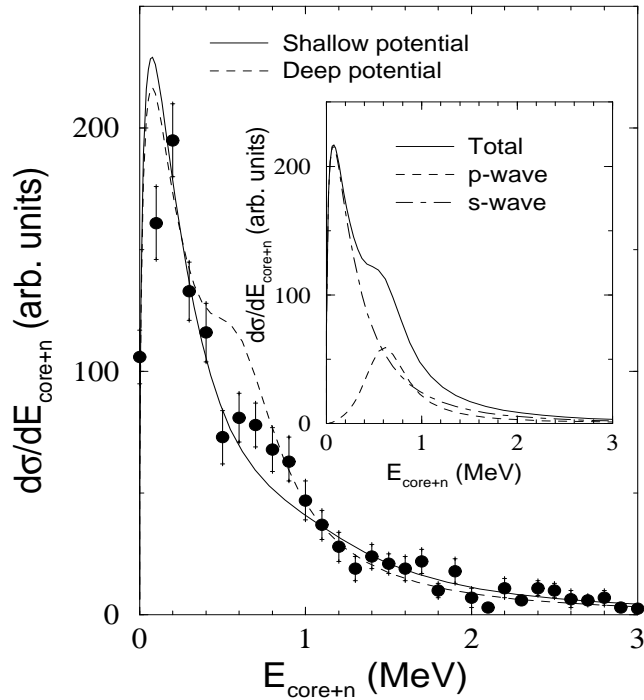


FIG. 15. The invariant mass spectrum for a ${}^{11}\text{Li}$ neutron removal reaction computed for both the shallow potential (solid curve) and the deep potential with one bound s-state (short-dashed curve) defined in the text. In the inset the case of the deep potential (solid curves) and the contributions from the s-waves (dot-dashed line) and the p-waves (dashed line) are shown. The experimental points for fast ${}^{11}\text{Li}$ (280 MeV/u) colliding with a carbon target are from [29].

of the momentum distributions at zero momentum. In fact, the value of the invariant mass spectrum divided by $\sqrt{E_{\text{core+n}}}$ is not zero at zero energy, and the lower the virtual s-state the larger the value at the origin. In the inset of fig. 15 we show the deep potential case where we have separated the contributions from the s and the p-waves. It is then clear how the s-wave is responsible for the first peak, while the shoulder is produced by the $p_{1/2}$ resonance at 0.77 MeV. The experimental points [29] correspond to a ^{11}Li fragmentation process on carbon. A better agreement between the computed curves and the experimental data is possible when the spin of the core is taken into account in the description of ^{11}Li and ^{10}Li .

VI. SUMMARY AND CONCLUSIONS

We study two prescriptions to take the Pauli principle into account in the three-body cluster model where more than one cluster contain nucleons. One is to exclude the Pauli forbidden two-body state from the active space available for the three-body system, the other is to construct a two-body potential without the Pauli forbidden state but with the same low energy properties.

We solve the Faddeev equations in coordinate space by means of the adiabatic hyperspherical expansion. We calculate the angular eigenvalues of the Faddeev equations which are closely related to the effective radial potentials. This spectrum is computed for the two different potentials with identical low energy properties and either without or with one Pauli forbidden bound s-state. Each bound state gives rise to a specifically behaving angular eigenvalue. The technically inexpensive prescription to account for the Pauli principle is then simply to omit the angular eigenvalue which corresponds to the Pauli forbidden bound state in the calculations of the three-body radial wave functions.

We apply these prescriptions to analyses of the high energy fragmentation reactions of two halo nuclei ^6He and ^{11}Li within a three-body neutron+neutron+core model. The potentials of the two prescriptions are adjusted to reproduce the same s- and p-wave low energy data.

For ^6He these data are known experimentally and the interactions are therefore fixed. The potential with forbidden state then gives correct binding energy and root mean square radius for ^6He . The equivalent potential without a bound state slightly underbinds the system. A small reduction of the repulsive core is needed to obtain the correct binding. This automatically provides almost the same reasonable root mean square radius. After this small adjustment the wave functions for the two nuclei for the two types of potential are compared and found remarkably similar.

For ^{11}Li we use the currently accepted experimental data for the lowest s- and p- levels in the neutron core subsystem to adjust the neutron core potentials. With these levels being close to experimental data the deep potentials provide reasonable binding energy and root mean square radius. The equivalent potential without a bound state slightly overbinds the system. After a small attenuation of the position of the neutron core $p_{3/2}$ level this prescription also provides the correct binding and size of the system.

In general the two prescriptions without any fine tuning provide very close but still distinguishable ground state properties of the three-body system. After small adjustments the properties become remarkably similar.

We then compute neutron and core momentum distributions in nuclear break-up reactions of these halo nuclei. We use the sudden approximation and include final state interactions, which are crucial for the neutron distributions as the full width at half maximum for the neutrons from ^6He is reduced by a factor of more than 2 from the value corresponding to omitting the final state interaction.

The two prescriptions give almost identical results and the measured momentum distributions are rather accurately reproduced. These computations are carried out in a consistent model where the same two-body potential is used both for the initial three-body halo structure and for the final state interaction after the break-up process.

The final state invariant mass spectra for ^5He and ^{10}Li are computed and their features discussed. A virtual s-state shows up as a pronounced peak close to zero energy. This peak arises from the phase space factor which vanishes at zero energy, and its position is unrelated with the energy of the virtual state. Higher angular momenta show up as distinct peaks at the resonance energy. These spectra are then sensitive to the continuum structure of the two-body system.

In conclusion the two prescriptions to account for the Pauli principle work remarkably well for the two test examples ^6He and ^{11}Li . In both cases the lowest Pauli forbidden s-state is occupied by nucleons in the core nucleus. However, the valence neutrons occupy predominantly neutron-core relative p-states and s-states, respectively for ^6He and ^{11}Li . The wave functions are further tested in connection with our fragmentation model and the measured momentum distributions are nicely reproduced. For ^6He these quantities are computed for the first time whereas ^{11}Li was investigated earlier in a more sophisticated model. Although fairly realistic, we used here only a schematic model, because the main purpose was to demonstrate the reliability to account for the Pauli principle. In any case the results provide additional support both for the prescriptions and for the fragmentation model.

Acknowledgments. We want to thank B. Jonson, K. Riisager, and H. Emling for useful discussions and for making the latest unpublished experimental data available. One of us (E.G.) acknowledges support from the European Union through the Human Capital and Mobility program contract nr. ERBCHBGCT930320.

- [1] Jean-Marc Richard, Phys. Rep. 212 (1992) 1
- [2] M.V. Zhukov, B.V. Danilin, D.V. Fedorov, J.M. Bang, I.J. Thompson and J.S. Vaagen, Phys. Rep. 231 (1993) 151
- [3] D.V. Fedorov, A.S. Jensen and K. Riisager, Phys. Rev. C49 (1994) 201
- [4] V.I. Kukulin and V.N. Pomerantsev, Ann of Phys. 111 (1978) 330
- [5] S. Marsh, Nucl. Phys. A389 (1982) 45
- [6] J. Bang, J.J Benayoun, C. Gignoux and I.J. Thompson, Nucl. Phys. A405 (1983) 126
- [7] L. Johannsen, A.S. Jensen and P.G. Hansen, Phys. Lett. B244 (1990) 357
- [8] D. Baye, Phys. Rev. Lett. 58 (1987) 2738
- [9] H. Fiedeldey, S.A. Sofianos, A. Papastilianos, K. Amos and L.J. Allen, Phys. Rev. C42 (1990) 411
- [10] T. Kobayashi, O. Yamakawa, K. Omata, K. Sugimoto, T. Shimoda, N. Takahashi and Tanihata, Phys. Rev. Lett. 60 (1988) 2599
- [11] E. Garrido, D.V. Fedorov and A.S. Jensen, Phys. Rev. C53 (1996) 3159
- [12] A.A. Korshennikov and T. Kobayashi, Nucl. Phys. A567 (1994) 97
- [13] D.V. Fedorov and A.S. Jensen, Phys. Rev. Lett. 71 (1993) 4103
- [14] D.V. Fedorov, A.S. Jensen and K. Riisager, Phys. Rev. C50 (1994) 2372
- [15] D.V. Fedorov, E. Garrido, and A.S. Jensen, Phys. Rev. C51 (1995) 3052
- [16] F. Ajzenberg-Selove, Nucl. Phys. A490 (1988) 1
- [17] Bohlen et al. Z.Phys. A344 (1993) 381
- [18] B.M. Young et al. Phys. Rev. C49 (1994) 279
- [19] M. Zinser et al., Phys. Rev. Lett. 75 (1995) 1719
- [20] S.N. Abramovich, B.Ya. Guzhovskij and L.M. Lazarev, Phys. Part. Nucl. 26 (1995) 423
- [21] T. Kobayashi, Nucl. Phys. A538 (1992) 343c
- [22] F. Humbert et al., Phys. Lett. B347 (1995) 198
- [23] T. Kobayashi, Nucl. Phys. A553 (1993) 465c
- [24] I.J. Thompson and M.V. Zhukov, Phys. Rev. C49 (1994) 1904
- [25] J.S. Al-khalili and J.A. Tostevin, Phys. Rev. Lett. 76 (1996) 3903
- [26] H. Geissel and W. Schwab, private communication
- [27] T. Nilsson et al., Europhys. Lett. 30 (1995) 19
- [28] P.G. Hansen, Proceedings International Conference on Exotic Nuclei and Atomic Masses (M. de Saint Simon and O. Sorlin, Arles, France, 1995), 175
- [29] H. Emling, private communication, and the S034 collaboration to be published